


Research Article

Study on the Earth-Covered Magazine Models under the Internal Explosion

Cheng Gong,¹ Yan-Yu Qiu ,² Zhi-Lin Long,³ Lu Liu,² Guan-Gan Xu,⁴ and Ling-Ming Yang¹

¹School of Mechanical Engineering and Mechanics, Xiangtan University, Xiangtan 411105, China

²State Key Laboratory of Disaster Prevention & Mitigation of Explosion & Impact, Army Engineering University of PLA, Nanjing 210007, China

³School of Civil Engineering, Xiangtan University, Xiangtan 411105, China

⁴School of Chemistry and Chemical Engineering, Nanjing University of Science and Technology, Nanjing 210094, China

Correspondence should be addressed to Yan-Yu Qiu; qiuyanyu78@sina.com

Received 13 June 2023; Revised 5 January 2024; Accepted 15 March 2024; Published 31 March 2024

Academic Editor: Yuanping Xu

Copyright © 2024 Cheng Gong et al. This is an open access article distributed under the Creative Commons Attribution License, which permits unrestricted use, distribution, and reproduction in any medium, provided the original work is properly cited.

The use of earth-covered magazines (ECMs) is increasingly prevalent in protective engineering due to their concealment and cost-effectiveness. To explore the optimal thickness of earth covering for ECMs, scaled model tests were conducted under explosive charges equivalent to 30 kilograms of TNT. The resulting overpressure outside the model in the 180° direction was measured. Subsequently, computational analyses were conducted employing LS-DYNA software to examine these experimental findings. The findings indicate that increasing the thickness of the rear soil can mitigate peak overpressure, delay the air shock wave's arrival time, and reduce the impulse of the positive phase. The numerical calculations closely align with experimental data, with peak overpressure deviation remaining under 10%. The shock wave initially impacts the top of the model before reaching the rear, with soil scattering more pronounced in the 90° direction compared to the 180° direction. Furthermore, an analysis of soil energy absorption rate variation was conducted based on energy conservation principles. These results provide valuable insights for optimizing the design and construction of ECMs.

1. Introduction

Also referred to as a semiunderground storage, this structure features top, sides, and rear coverage with soil, while the front wall is equipped with entrances and exits. It is commonly utilized for storing explosive materials and ammunition [1]. With urban areas expanding continuously, adjacent buildings often surround ammunition depots. Given the occasional internal explosion risks within ammunition depots and the insufficient safety distance between neighboring structures, it becomes imperative to devise methods for minimizing the shock wave impact radius. Such measures offer crucial direction for designing weapons and ammunition storage facilities.

Experimental studies on earth-covered magazines trace back to 1945, notably with the Igloo Magazine tests conducted in Arco, Idaho. These endeavors aimed to establish

safe distances while conserving land resources [2, 3]. These tests distinctly focused on examining the overall structural response, air explosion measurements, and the density and distribution patterns of debris. Determining the closest safe distance between the earth-covered magazines was guided by assessing debris dispersion and overpressure peaks resulting from internal explosion tests.

Existing research suggests that the strength and thickness of the earth covering are the crucial factors in mitigating external shock wave. Kingery et al. [4] conducted 1:50 scaled internal explosion tests on earth-covered magazine models, meticulously examining the impact of varying soil cover thickness above the model on the external air pressure in the 0°, 90°, and 180° directions. The findings reveal that augmenting the soil layer thickness does not lead to increased air pressure in the 0° direction, while the alteration pattern of air pressure in the 90° remains inconspicuous, and

the decay of air pressure in the 180° direction intensifies. Nonetheless, Charles' experimental inquiry primarily focuses on the thickness of earth cover above the magazine, with scant exploration into the influence of changes in earth cover thickness behind the magazine on external pressure and positive pressure impulse. Moreover, Charles' experimental results indicate that the pressure sensors were susceptible to high temperatures and light, resulting in numerous missing experimental data points. Consequently, in this study, to reduce the influence of light and heat on the pressure sensors, protective measures include shielding the sensors with aluminum film and applying silicone grease.

The United States Department of Defense (DOD) standard [5] highlights a pressure reduction of approximately 66.7% within an earth-covered magazine equipped with protective shielding. Similarly, according to the Chinese Standard [6], installing protective barriers around the earth-covered magazine is recommended to achieve a maximum reduction in external pressure of 60%. Beppu et al. [7] conducted experiments on earth-encased magazines with protective barriers on their front walls, observing that increased soil thickness alters the distribution of external pressure. As the depth of the soil increases, the intensity of the shock wave decreases at the rear. Liu et al. [8] and Li et al. [9] analyzed the factors influencing the safety distance of earth-covered magazine, emphasizing the mitigating effect of soil on shock wave overpressure and its efficacy in blocking structural debris pathways. Furthermore, Xu et al. [10, 11] conducted scaled tests on earth-covered magazines to investigate overpressure and debris distribution in various directions. These findings were integrated with numerical simulations to estimate the distance that concrete fragments would project.

The German military [12] conducted an internal explosion tests within earth-covered ISO containers to ascertain safe distances and debris ranges between adjacent containers. Results revealed that pressure relief and debris distribution predominantly occurred in the container's frontal area, with a notable reduction in debris range facilitated by soil mounding at the container's front. Tian and Deng [13] explored the influence of earth covering thickness on structural dynamic responses and shock wave overpressure propagation in underground structures subjected to internal explosions. Findings indicate that earth covering thickness impacts the structure's dynamic response to some extent, while shock wave propagation during internal explosions exhibits complexity, with overpressure diminishing as the proportional distance from the blast center increases. Wang [14] investigated the impact of ground blast shock waves on soil dynamic properties using a combination of experiments and numerical simulations. Destructive effects leading to the deformation and destruction of external protective soil layers were analyzed.

Numerous scholars [15–19] have extensively studied the dynamic mechanical characteristics and energy dissipation behaviors of soils under varying strain rates, utilizing a combination of experiments and numerical simulations. Liu and Chen [20] examined the specific energy absorption of compacted cohesive soils under different strain rates and

water contents, employing SHPB (split Hopkinson pressure bar) test equipment. Ma et al. [21] investigated the energy dissipation properties of frozen sandy soils across various deformation stages via split Hopkinson pressure bar tests, revealing close correlations between energy dissipation parameters and moisture content, temperature, and strain rate. Alekseenko and Rykov [22] analyzed the impact of detonation location on the distribution of blast energy in soil, employing physical parameters such as axial stress and impulse as indicators. Grujicic et al. [23] and Grujicic et al. [24] investigated the explosion process within soils under varying water content conditions, combining experimental approaches with numerical simulations. Their findings indicate that low porosity and high saturation soils exhibit effective energy absorption capabilities.

In summary, while numerous scholars have primarily concentrated their research on internal pressure distribution and structural response resulting from internal explosions, there remains a paucity of studies on the effects of internal explosions within earth-covered magazines on induced damage to external surroundings, particularly concerning the propagation of pressure externally and the impact of earth covering thickness. In this work, internal explosion tests were performed using four scaled models of earth-covered magazines. Pressure data in 180° direction and soil scattering were acquired utilizing pressure sensors, high-speed camera, and unmanned aerial vehicles (UAVs). Additionally, the simulation of internal explosions within the models was conducted using the LS-DYNA software. The study evaluated the influence of soil on explosive shock wave energy absorption and proposed the most suitable design value for rear soil thickness. The findings offer valuable insights for engineering applications, providing guidance for optimizing earth-covered magazine designs and enhancing their protective capabilities.

2. Experimental Set-Up

2.1. Models. Swisdak et al. [25] conducted explosion tests in earth-covered magazines, revealing that both reinforced concrete and masonry structures are destroyed when subjected to explosions with large charges. Additionally, Xiong's research [26] demonstrated that under high loading densities of 30 kg/m³, all reinforced concrete (RC) structures disintegrate, with minimal impact on structural integrity from the soil cover under such conditions. Therefore, in this study, structural strength considerations are disregarded, and high-density polyethylene (HDPE) pipes are utilized to represent the most unfavorable scenario. Half-round HDPE pipes were employed to construct circular arches, serving as the support system for the earth-covered magazine. These pipes are covered with sandy soil above and behind them to replicate the soil's attenuation effect on shock waves in the absence of concrete, representing the most unfavorable condition. It is important to note that HDPE pipe material possesses low strength and is directly damaged by explosive forces, thus exerting negligible influence on shock wave propagation in the soil. The sand utilized ranges $4.55 \times 10^{-5} \sim 2 \times 10^{-5}$ m, with a density of 1.78 g/cm³. Due to

constraints such as the test site limitations, time, cost, and safety considerations, the explosion prototype test is conducted within manageable parameters. Smith et al. [27] demonstrated that scaled internal explosion tests can yield reliable data, especially concerning peak overpressure, even at reduced scales. Similarly, Yang et al. [28] established numerical simulation models of different proportions to simulate explosions in confined spaces. Their findings suggest that scaled experimental results closely mirror those of the original model, allowing for accurate prediction of explosion damage effects in the original structure.

Yang's research [28] indicates that the primary influence on overpressure from internal explosions is determined from the following parameters:

- (1) Air properties: initial pressure (p_0), air density (ρ_a), air adiabatic index (γ_a);
- (2) Explosive characteristics: mass (W), density (ρ_e), energy released per unit mass (e), and explosion product expansion index (γ_e);
- (3) Structure attributes: length (l), width (b), height (h), strength (σ), Young's modulus (E), and material density (ρ_s);

- (4) The distance (R) from the measurement point to the source of the explosion.

Citing the principle of similarity [29], the fundamental dimensions of mass (M), length (L), and time (T) are employed as the primary dimensions, as detailed in Table 1, to encapsulate the dimensional characteristics of each parameter. The relationship between explosion overpressure inside the structure and its influencing factors is described as follows:

$$P = f(W, p_0, \rho_a, \gamma_a, \rho_e, e, \gamma_e, l, b, h, \sigma, E, \rho_s, R). \quad (1)$$

Given that E is not an independent factor for the same structural material, it can be omitted, along with γ_a and γ_e , which are dimensionless quantities. Hence, equation (1) simplifies to

$$P = f(W, p_0, \rho_a, \rho_e, e, l, b, h, \sigma, \rho_s, R). \quad (2)$$

Revising equation (2) to incorporate W , ρ_a , and σ as basic quantities, we obtain

$$\frac{P}{\sigma} = f \left[\frac{p_0}{\sigma}, \frac{\rho_e}{\rho_a}, \frac{e}{\sigma/\rho_a}, \frac{l}{(W/\rho_a)^{(1/3)}}, \frac{b}{(W/\rho_a)^{(1/3)}}, \frac{h}{(W/\rho_a)^{(1/3)}}, \frac{\rho_s}{\rho_a}, \frac{R}{(W/\rho_a)^{(1/3)}} \right]. \quad (3)$$

Under identical charge type and air conditions, with the structural material remaining consistent, if $(W_p^{(1/3)}/W_m^{(1/3)}) = (l_p/l_m) = (b_p/b_m) = (h_p/h_m) = (R_p/R_m) = \lambda$, $p_p = p_m$. Here, p refers to the prototype and m denotes the model, while λ represents the scaling ratio.

Hence, the dimensions of the test model structure were scaled down based on a prototype structure, illustrated in Figure 1. For security reasons, the specifics of the prototype structure are undisclosed. In accordance with the stipulations outlined in the standard [6], the test incorporated four variations of rear soil thickness, detailed in Table 2.

2.2. Experimental Instruments and Equipment. The experimental instrumentation comprised pressure sensors, electricity provision setups, oscilloscopes, signal conditioning apparatus, and data collection systems. Figure 2 illustrates the detailed sensor layout diagram, utilizing Swiss KISTLER6233 pressure sensors. These sensors, with the resonance frequency of 500 kHz, featured a range of 0.17–6.9 MPa. Signal acquisition from the pressure sensors occurred via signal acquisition occurred through the pressure sensors via the data acquisition tool, operating at a sampling rate of 1 MHz. Eleven sensors were strategically positioned along the 180° direction at specified distances from the blast center, as outlined in Table 3. Each sensor was securely fixed to a bracket via a casing pipe and horizontally adjusted for optimal positioning, as depicted in Figure 3. To minimize interference during testing, the bracket was buried

50 cm below the ground surface and secured with nails. An unmanned aerial vehicle (UAV) and a high-speed camera were used to document the test procedures, capturing vital data on soil scattering and shock wave propagation.

A box bulk TNT charge, with a density of 0.9 g/cm³ and a total equivalent TNT mass of 30 kg, was selected as the explosive. To expedite the detonation process, an electrical initiator was employed to activate the RDX explosive column, subsequently causing the detonation of the TNT explosive. Positioned centrally, the explosive was depicted as shown in Figure 4.

3. Experiment Results

3.1. Pressure Parameters. Figure 5 illustrates the pressure-time histories of case number 1 recorded by the sensor, with data processing conducted to derive shock wave-related parameters as presented in Table 4 (blank sections indicate missing or abnormal data). Additionally, Figure 6 depicts a typical pressure-time history. Comparing the rear soil thickness of 30 mm to increased thickness of 60 mm, 150 mm, and 300 mm, when the scaled distance is small, pressure decreased by 19.07%, 25.04%, and 22.58%, respectively, while the shock wave arrival time was prolonged by 6.35%, 7.93%, and 5.86% and the positive phase impulse reduced by 7.62%, 6.61%, and 5.26%, respectively. For larger scaled distances, the pressure decreases by 36.34%, 44.20%, and 37.71%, respectively, with essentially the same shock wave arrival time. Furthermore, the positive phase impulse decreases by 23.50%, 32.29%, and 17.43%, respectively.

TABLE 1: Parameters and dimensions for internal explosion.

Parameter	Dimension
P	$ML^{-1}T^{-2}$
t	T
W	M
P_0	$ML^{-1}T^{-2}$
ρ_a	ML^{-3}
γ_a	1
ρ_e	ML^{-3}
e	L^2T^{-2}
γ_e	1
l	L
b	L
h	L
σ	$ML^{-1}T^{-2}$
E	$ML^{-1}T^{-2}$
ρ_s	ML^{-3}
R	L

Using the peak overpressure equation for near-surface blast air summarized by Baker [30], the pressure-scaled distance and positive phase impulse-scaled distance were

$$\left\{ \begin{array}{l}
 d = 30\text{mm}: y = \frac{121.988}{x} + \frac{-74.143}{x^2} + \frac{243.913}{x^3}, \quad R^2 = 99.72\%, \\
 d = 60\text{mm}: y = \frac{76.114}{x} + \frac{16.816}{x^2} + \frac{132.285}{x^3}, \quad R^2 = 99.75\%, \\
 d = 150\text{mm}: y = \frac{72.749}{x} + \frac{87.501}{x^2} + \frac{2.510}{x^3}, \quad R^2 = 99.71\%, \\
 d = 300\text{mm}: y = \frac{64.673}{x} + \frac{143.805}{x^2} + \frac{-57.193}{x^3}, \quad R^2 = 99.83\%, \\
 \\
 d = 30\text{mm}: y = \frac{41.911}{x} + \frac{-47.202}{x^2} + \frac{16.176}{x^3}, \quad R^2 = 99.67\%, \\
 d = 60\text{mm}: y = \frac{34.624}{x} + \frac{-29.616}{x^2} + \frac{4.281}{x^3}, \quad R^2 = 99.35\%, \\
 d = 150\text{mm}: y = \frac{40.781}{x} + \frac{-53.054}{x^2} + \frac{31.936}{x^3}, \quad R^2 = 99.45\%, \\
 d = 300\text{mm}: y = \frac{37.594}{x} + \frac{-41.037}{x^2} + \frac{15.391}{x^3}, \quad R^2 = 99.66\%.
 \end{array} \right. \quad (4)$$

3.2. Soil Scattering. It was observed that soil scattering after detonation was not uniform displaying significant non-uniform characteristics. Soil accumulation from all tests concentrated within a T-shaped area spanning $\pm 90^\circ$ and 180° . Figure 9, captured by high-speed cameras and UAVs, depicts soil scattering and accumulation in Case 1. Analysis indicates that initially, the model's inherent strength

obtained from experimental data and plotted in double logarithmic coordinates (see Figures 7 and 8). As depicted in equations (1) and (2), each dataset was represented by a fitting function $y = (A/x) + (B/x^2) + (C/x^3)$ with a confidence level exceeding 99%. Notably, for the thicknesses of 60 mm, 150 mm, and 300 mm, all exhibited a consistent trend in overpressure. However, upon comparing the impulse, it was found that in larger scaled distances, the minimum impulse occurred with a thickness of 60 mm. Hence, further analysis is warranted.

characteristics combined with the blast release at 0° led to radial blast load on the arch structure, causing outward rupture. This resulted in soil being thrown radially, forming a scattering plane at $\pm 90^\circ$, while soil at the rear of the model was driven backward, forming a 180° scattering plane. The soil dispersed in both directions, forming the T-shaped accumulation belt captured by the UAV.

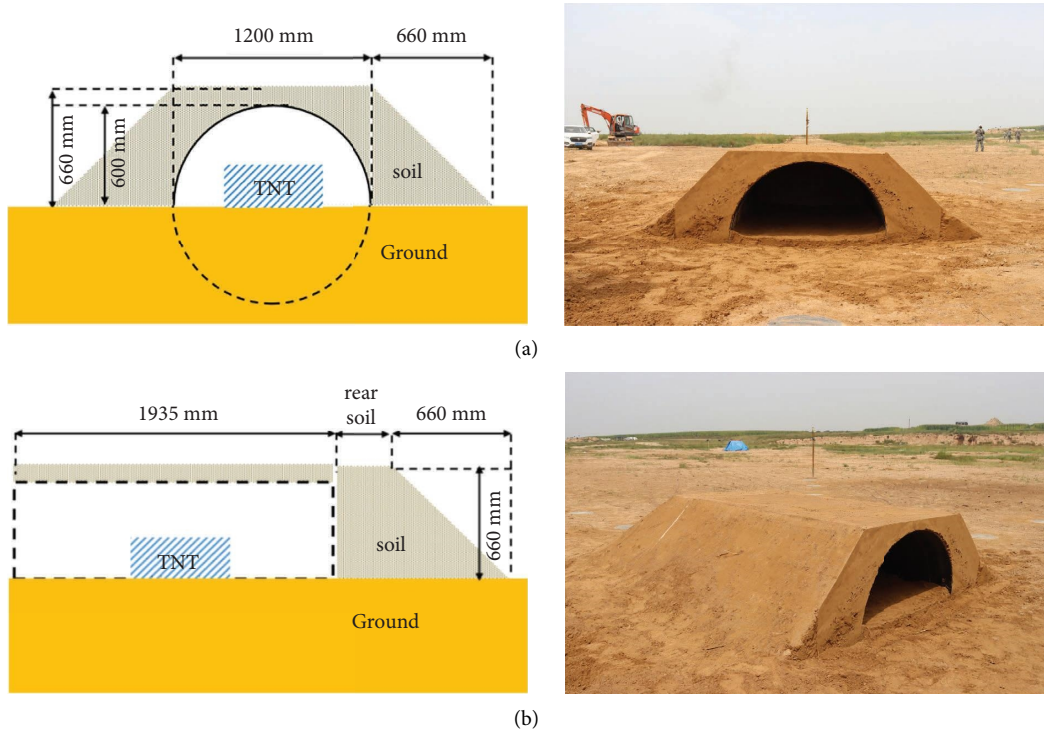


FIGURE 1: Earth-covered magazine model. (a) Model front view. (b) Model side view.

TABLE 2: Cases.

Number	Rear soil thickness (mm)	TNT equivalent (kg)	Explosive size (mm)
1	30		
2	60		
3	150	30	850 × 280 × 140
4	300		

TABLE 3: The distance from the measuring points of the blast center.

Point number	Scaled distance (m/kg ^{1/3})	Actual distance (m)
1	1.60	4.97
2	2.18	6.77
3	2.95	9.17
4	3.60	11.19
5	4.67	14.51
6	5.60	17.41
7	7.30	22.68
8	11.82	36.73
9	16.24	50.46
10	23.26	72.27
11	29.29	91.01

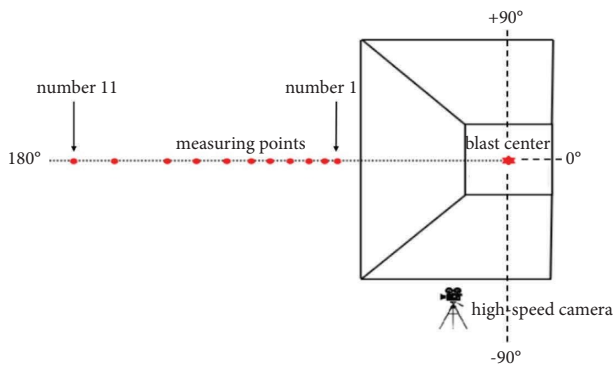


FIGURE 2: Layout of measuring points.

4. Numerical Simulation

To investigate the impact of rear soil thickness on external pressure propagation, numerical simulation proves to be the prevalent and efficacious method. In this investigation, we utilized LS-DYNA finite element simulation software,



FIGURE 3: Sensor placement.

employing a fluid-structure interaction algorithm. This allowed us to calculate the temporal profiles of air pressure outside the model and track the process of soil scattering.



FIGURE 4: Explosive and placement.

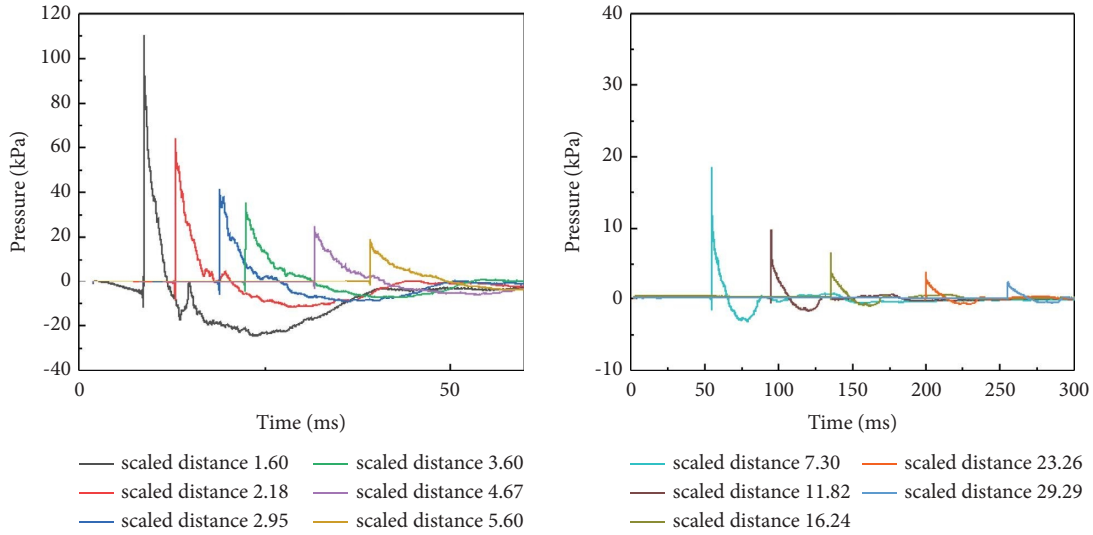


FIGURE 5: Pressure-time histories.

4.1. Finite Element Model. To explore the effects of explosions, numerical analysis tools must ensure coupling between hydrodynamic states and solids. Built upon the principles of continuum mechanics, LS-DYNA, a nonlinear finite element analysis program, utilizes explicit time integration methods to capture dynamic mechanical behaviors with precision. This approach enables the study of instantaneous explosion dynamics, albeit requiring controlled time step (Δt) for stable calculations.

Effective employment of explicit time integration relies heavily on selecting an appropriate time step. Specifically, ensuring a time step smaller than the critical time interval, which is determined by the time step control factor (TSSFAC), is essential for stability. LS-DYNA automatically partitions time (T) into $T/\Delta t$ intervals. The program manual recommends setting the time step control factor within the range of 0.1~0.9, with a value lower than 0.67 suggested for explosion analysis [31].

$$\Delta t = \text{TSSFAC} \cdot \frac{l_{\text{mesh}}}{C_l}, \quad (5)$$

where l_{mesh} represents the minimum mesh dimension and C_l denotes the wavelength.

For computational convenience, a symmetric structure was simulated, employing a half-model approach. The software was used to construct models for air, explosives, pipes, and soil. The numerical simulation involved a fluid-structure coupling algorithm, with the Euler mesh utilized for air and explosives, and the Lagrangian mesh employed for pipes. This method combines the benefits of the Lagrangian method and the Eulerian method, addressing material deformation and moving boundary complexities [32–35]. During explosion, significant soil deformation occurs. Establishing a solid element mesh may result in negative volume generation, leading to substantial errors or halting the calculation.

The soil characterization is established utilizing the keyword `*INITIAL_VOLUME_FRACTION_GEOMETRY`, facilitating modeling of complex structures and meshing. The grid size of the soil is determined by `*NTRACE`, set to 17, resulting in subdivision of the ALE element into 353 regions. It is crucial to ensure the air region is sufficiently large to capture a complete pressure-time curve when soil reaches the air boundary, causing a sudden decrease in step size. Nonreflection boundaries are established at air boundaries, except for the symmetry plane and ground. The

TABLE 4: Shock wave-related parameters.

Rear soil thickness (mm)	Scaled distance (m/kg ^{1/3})	Peak overpressure (kPa)	Time of arrival (ms)	Positive pressure duration (ms)	Positive phase impulse (kPa·ms × 10 ⁻⁵)
30	1.60	107.08	8.71	3.16	11.68
	2.18	63.12	12.95	5.24	11.01
	2.95	41.72	18.89	8.05	8.98
	3.60	35.27	22.38	9.01	8.68
	4.67	25.14	31.69	9.44	7.06
	5.60	19.18	39.31	10.05	5.98
	7.30	18.94	54.68	10.70	4.86
	11.82	9.23	94.87	11.94	3.12
	16.24	6.27	136.61	12.58	2.45
	23.26	3.64	201.08	13.45	1.78
	29.29	2.62	259.16	14.11	1.43
60	1.60	86.66	9.26	3.36	11.11
	2.18	50.74	13.65	4.90	10.17
	2.95	31.52	19.74	4.93	7.96
	3.60	27.02	23.31	9.72	7.97
	4.67	—	—	—	—
	5.60	16.06	40.54	11.06	5.25
	7.30	11.95	56.12	11.32	4.19
	11.82	5.33	97.04	12.4705	2.64
	16.24	3.42	137.63	12.98	1.94
	23.26	2.33	203.60	14.11	1.43
	29.29	1.67	259.55	14.55	1.10
150	1.60	80.26	9.40	3.79	12.66
	2.18	52.46	13.80	5.35	10.28
	2.95	33.05	19.87	9.28	8.94
	3.60	28.06	23.43	9.58	8.22
	4.67	18.88	32.90	10.09	6.97
	5.60	17.34	40.63	10.85	5.78
	7.30	13.06	56.14	11.52	4.68
	11.82	6.26	96.96	12.88	2.91
	16.24	3.56	137.47	13.60	2.05
	23.26	2.16	203.28	14.89	1.38
	29.29	1.46	259.33	14.93	0.97
300	1.60	82.93	9.22	3.08	11.15
	2.18	53.42	13.57	5.10	10.43
	2.95	35.82	19.57	5.03	8.24
	3.60	29.46	23.10	9.90	7.57
	4.67	—	—	—	—
	5.60	16.06	40.18	12.87	5.53
	7.30	12.37	55.74	13.10	4.52
	11.82	5.31	96.61	13.75	2.89
	16.24	3.33	137.16	15.50	2.35
	23.26	2.32	203.01	14.80	1.55
	29.29	1.63	258.78	15.68	1.18

earth-covered magazine model restricts vertical displacement only at the bottom surface. The symmetry boundary is applied at the symmetry plane, and the keyword `LOAD_BODY_Z` simulates the effect of gravity. Nonreflection boundaries are set at air boundaries, except for the symmetry plane and ground. The earth-covered magazine model restricts vertical displacement only at the bottom surface. At the symmetry plane, the symmetry boundary is implemented, and the keyword `LOAD_BODY_Z` simulates the effect of gravity.

To ensure grid convergence, we chose six element sizes for the model, varying from 5 mm to 20 mm. The soil element size matched that of the air element. Figure 10 illustrates the relative error between numerical simulation and experimental air pressure values at different earth covering thicknesses and air element sizes. As the element size decreases, the relative error diminishes, albeit with increased computational time. Balancing computational efficiency and relative error, an element size of 12.5 mm is recommended, also applied to the circular pipe unit size. The

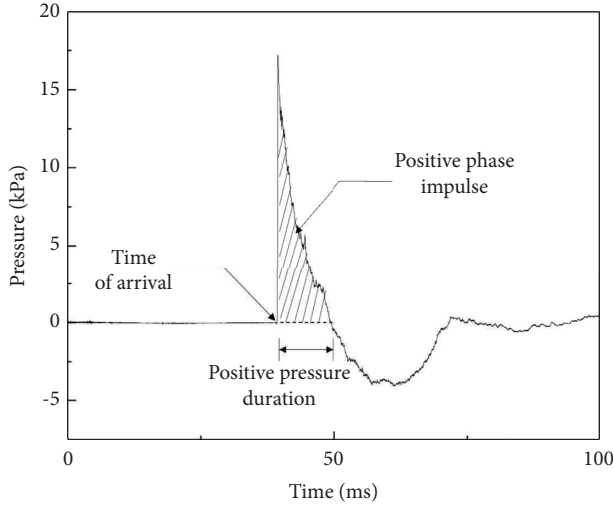


FIGURE 6: Typical pressure-time history.

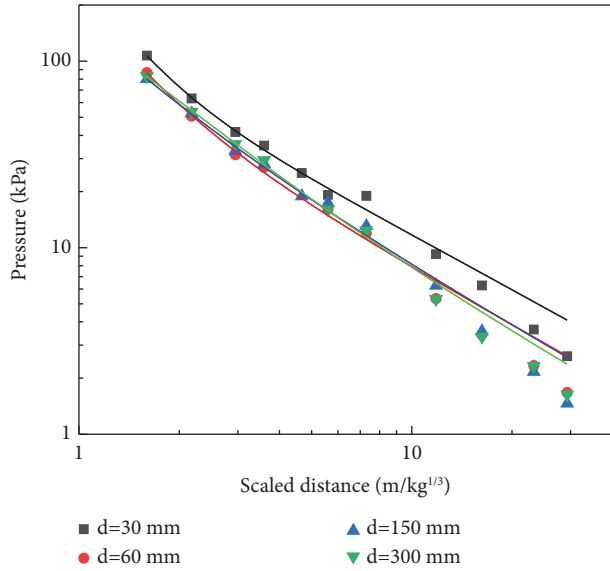


FIGURE 7: Pressure-scaled distance fitting curve.

air model dimensions were $5250 \times 1600 \times 5200$ mm, while the TNT model dimensions were $450 \times 100 \times 200$ mm. Figure 11 depicts the model diagram with a rear soil thickness of 30 mm. As the element size decreases, the relative error diminishes, albeit with increased computational time.

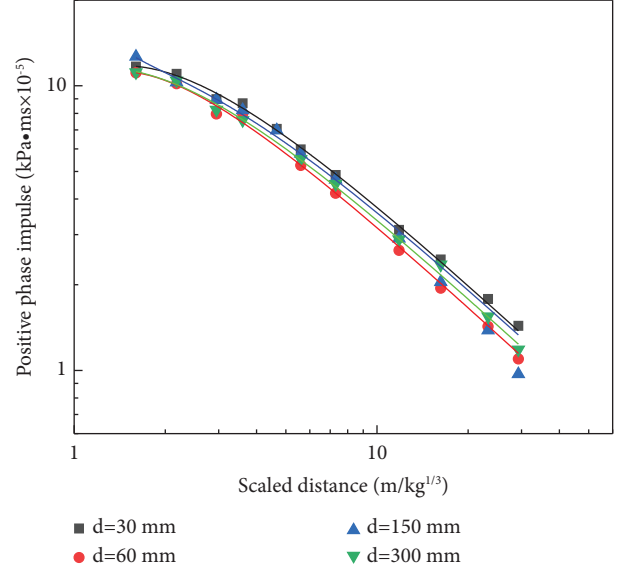


FIGURE 8: Impulse-scaled distance fitting curve.

4.2. Material Properties. The material's internal constitutive law establishes how the stress tensor correlates with the strain tensor. Additionally, following external force impact, pressure, temperature, density, internal energy, and volume changes are interrelated, as elucidated by the equation of state (EOS). For accurate analysis of explosion phenomena, matching the appropriate equations of state with the material ensures dynamic response and volume change alignment following exposure to explosion forces.

The characterization of air properties employs the *MAT_NULL material model combined with the EOS_LINEAR_POLYNOMIAL polynomial equation of state [31], which is formulated as

$$P = C_0 + C_1\mu + C_2\mu^2 + C_3\mu^3 + (C_4 + C_5\mu + C_6\mu^2)E, \quad (6)$$

$$\mu = \frac{1}{V_1} - 1.$$

In this equation, P represents the gas pressure and C_0 to C_6 denote the state parameters. For this model, $C_0 = C_1 = C_2 = C_3 = C_6 = 0$ and $C_4 = C_5 = 0.4$. Denoted as E , the internal energy of the gas is set at $2.5 \times 10^5 \text{ J/m}^3$, and V_1 represents the relative volume, which is assumed to be 1.0.

The *MAT_HIGH_EXPLOSIVE_BURN model characterizes the explosive material, coupled with the EOS_JWL polynomial equation of state [31], which is formulated as

$$P = A \left(1 - \frac{\omega}{R_1 V} \right) e^{-R_1 V} + B \left(1 - \frac{\omega}{R_2 V} \right) e^{-R_2 V} + \frac{\omega E}{V} P = A \left(1 - \frac{\omega}{R_1 V} \right). \quad (7)$$

In this equation, P represents the pressure, while the material parameters A , B , R_1 , and R_2 hold the values of 3.712×10^{11} , 3.23×10^9 , 4.15, and 0.95, correspondingly. The

internal energy per unit volume, denoted by E , is prescribed as $7 \times 10^9 \text{ J/m}^3$, and V represents the relative volume, assumed to be 1.0.

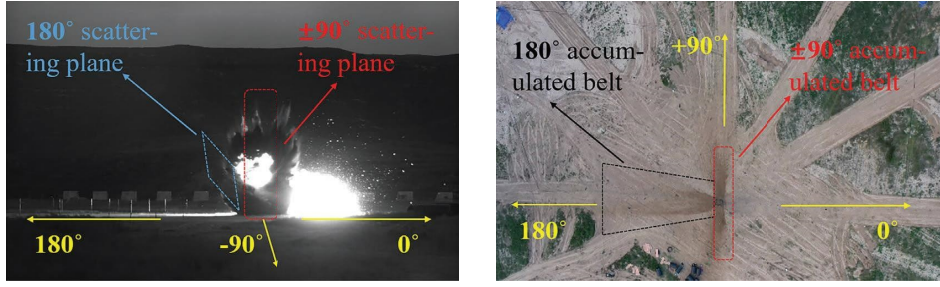


FIGURE 9: The scattering and accumulation of soil.

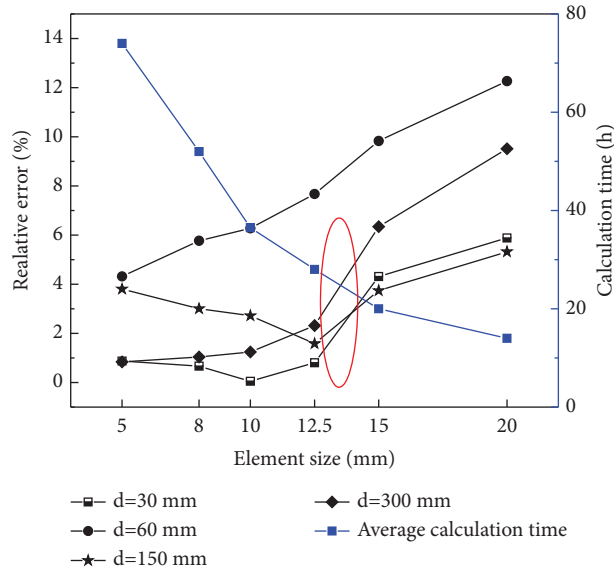


FIGURE 10: The effect of mesh size.

The mechanical properties of HDPE material are viscoelastic, affected by stress, deformation, temperature, and time. Temperature effects on HDPE materials are disregarded in this study, indicating their mechanical properties are strain rate-dependent. Therefore, the *MAT_PLASTICITY_POLYMER model employed herein characterizes the dynamic response of polymers under high strain rates, with material parameters outlined in Table 5.

To accurately simulate the crushing or compacting behavior of the pore material and its dynamic response postexplosion, the soil constitutive law must be precise. This study utilizes the *MAT_SOIL_AND_FOAM_FAILURE model, tailored for soil and foam calculations, aligning with material calculations [31]. The material is constitutively modeled as follows:

$$\phi = J_2 - [a_0 + a_1 p + a_2 p^2]. \quad (8)$$

In this constitutive model, ϕ denotes the partial ideal plastic yield function, J_2 represents the second stress invariant, $J_2 = (1/2)S_{ij}S_{ij}$, S_{ij} denotes the deviatoric stress tensor, and $J_2 = (1/3)\sigma_y^2$, where σ_y is the uniaxial yield stress on the yield surface. a_0 , a_1 , and a_2 are constants; p denotes the pressure. In cases where the material's yield

strength is disregarded, $\phi = 0$. A summary of material parameters can be found in Table 6.

$$a_0 = \frac{1}{3}\sigma_y^2, a_1 = 0, a_2 = 0. \quad (9)$$

5. Numerical Results and Discussion

5.1. Overpressure. The numerical methodologies, material parameters, and numerical models were validated by integrating them with experimental data. Ground explosion experiments were conducted to measure air overpressure, verifying the numerical analysis results and providing a reliable numerical model for ECM analysis.

Due to the limited size of the air grid, data comparison is restricted to the first measurement point. Figure 12 illustrates the comparison of pressure between experimental and simulation results at a scaled distance of $1.6 \text{ m/kg}^{1/3}$. The relative error (%) was calculated using the following formula: (numerical analysis value – experimental measurement value)/experimental measurement value $\times 100\%$.

Table 7 demonstrates that with the exception of specific cases with significant positive pressure duration error, the remaining data errors are within 10%. Despite some

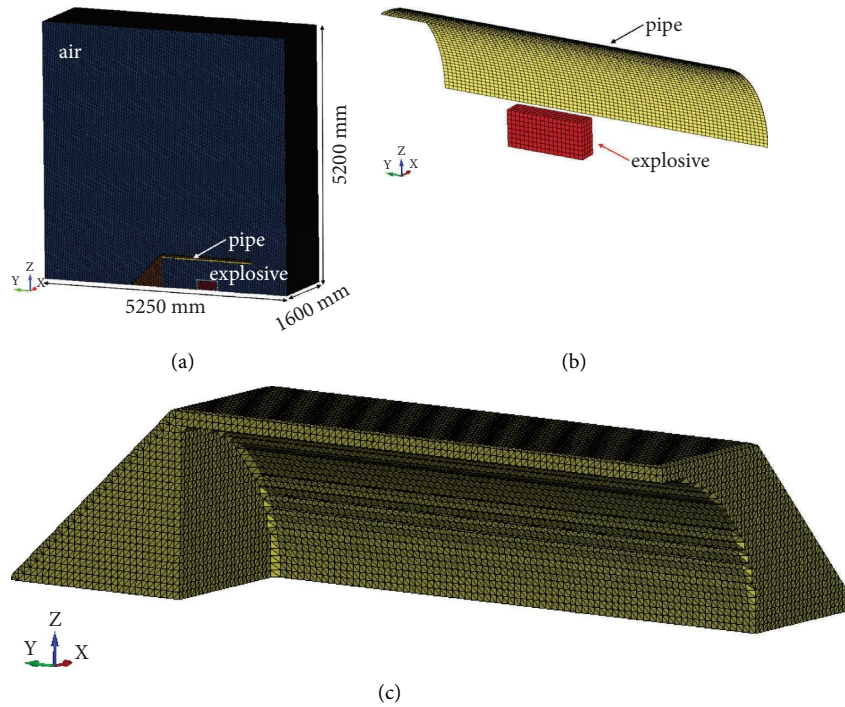


FIGURE 11: The numerical simulation model. (a) Geometry of the model. (b) Finite element mesh of pipe and explosive. (c) Finite element mesh of soil.

TABLE 5: Material parameters of the pipe [36].

Density (g/cm^3)	Young's modulus (GPa)	Poisson's ratio	Tensile strength (MPa)
0.936	0.8349	0.46	31.6

TABLE 6: Material parameters of the soil [37].

Density (g/cm^3)	Shear modulus (GPa)	Bulk modulus (GPa)	A0	A1	A2	PC (GPa)	VCR	REF
1.80	0.0638	30.0	$3.40E-9$	$7.033E-5$	0.30	$6.90E-6$	0.0	0.0

discrepancies, these error values fall within acceptable limits. The divergence between experimental findings and numerical analysis results primarily stems from the inherent nonuniformity, nonlinearity, and dynamic fluctuations in materials, geometries, environmental conditions, and contact properties that are integral to the analysis of shock effects. Additionally, in finite element analysis of instantaneous dynamics, it is imperative to ensure that material parameters are consistent with the evolving behavior observed in the material, which encompasses variations in internal energy, temperature, pressure, and volume as dictated by the EOS. The meshed model also played a significant role in the numerical calculations. Overall, these findings suggest good agreement between experimental and numerical models, affirming the suitability of the numerical model for further analysis. Moreover, the results validate the effectiveness of using the ALE fluid-structure coupling algorithm to examine the dynamic attributes of the explosion phenomenon [38–41].

5.2. Damage Characteristics of the Pipe. Figure 13 illustrates the destruction process of the pipe with a soil cover thickness of 30 mm. Upon detonation of the explosive, a spherical blast wave rapidly forms, exerting pressure on the top and sides of the pipe at approximately 0.12 ms. As the soil's wave impedance is lower than that of the pipe, a segment of the compressive pulse reaching the pipe's surface is transmitted into the soil, while the remainder reflects as a tensile wave. By 0.33 milliseconds, the tensile stress induced by this wave surpasses the pipe's dynamic tensile strength, resulting in cracks forming on both the upper and lateral surfaces. Over time, the blast wave's area of influence expands, and deformation propagation shifts gradually from the pipe's center towards both ends. The constrained elements at the pipe-soil interface experience significant deformation, culminating in failure as depicted in Figure 13(e). The predominant damage distribution centers around the explosive located at the midpoint of the pipe, extending outward in a radial fashion. Notably, the top and side positions of the

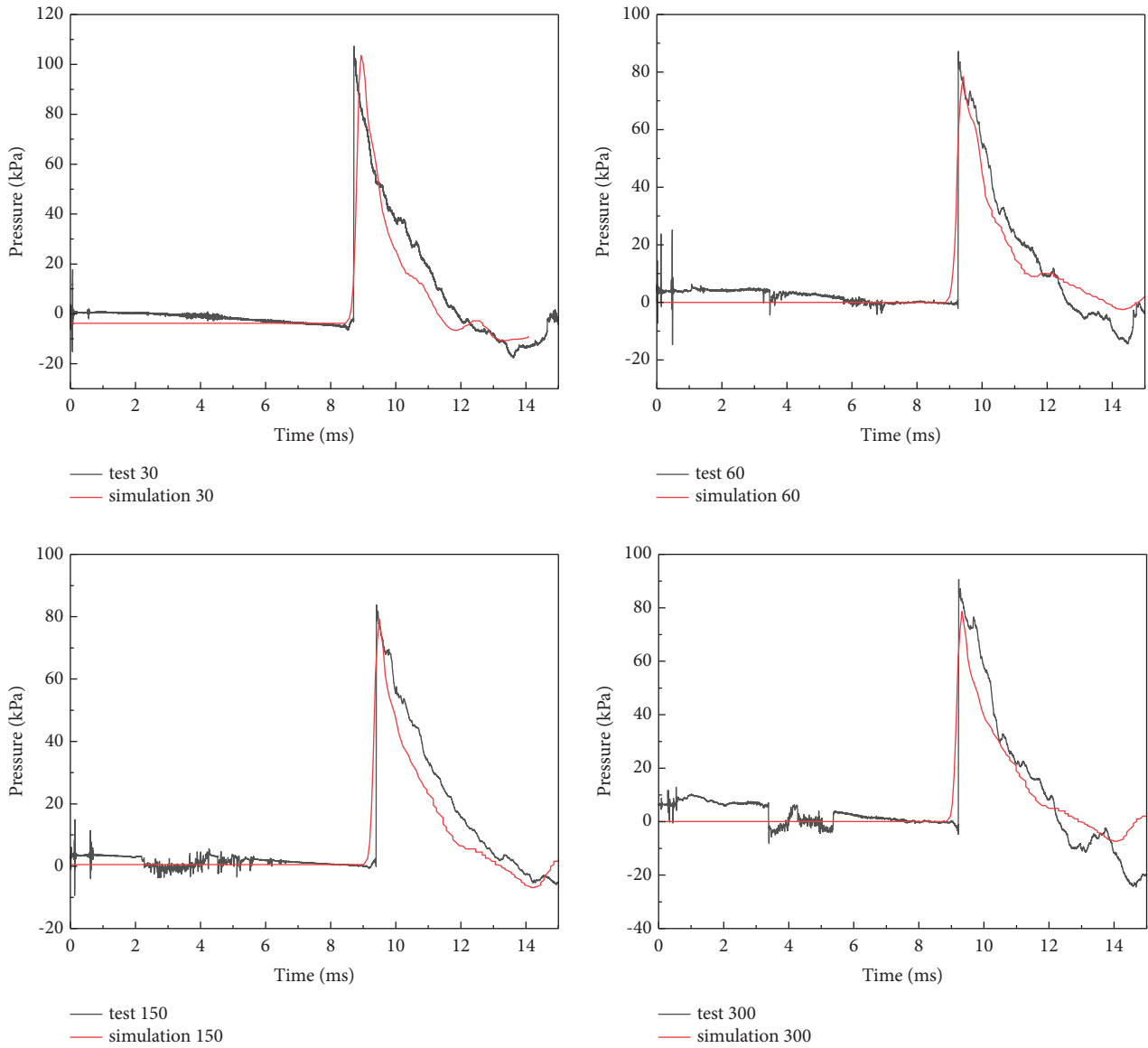


FIGURE 12: Comparison of test and numerical simulation.

TABLE 7: Comparison of test and numerical simulation.

Rear soil thickness (mm)	Parameter	Test	Simulation	Relative error (%)
30	Peak overpressure (kPa)	107.08	103.57	3.28
	Time of arrival (ms)	8.71	8.51	2.30
	Duration (ms)	3.16	3.01	4.75
60	Peak overpressure (kPa)	86.67	78.40	9.54
	Time of arrival (ms)	9.26	8.88	4.10
	Duration (ms)	3.36	4.55	35.42
150	Peak overpressure (kPa)	80.26	79.18	1.35
	Time of arrival (ms)	9.40	9.02	4.04
	Duration (ms)	3.79	4.04	6.60
300	Peak overpressure (kPa)	82.93	78.67	5.14
	Time of arrival (ms)	9.22	8.85	4.01
	Duration (ms)	3.08	4.04	31.17

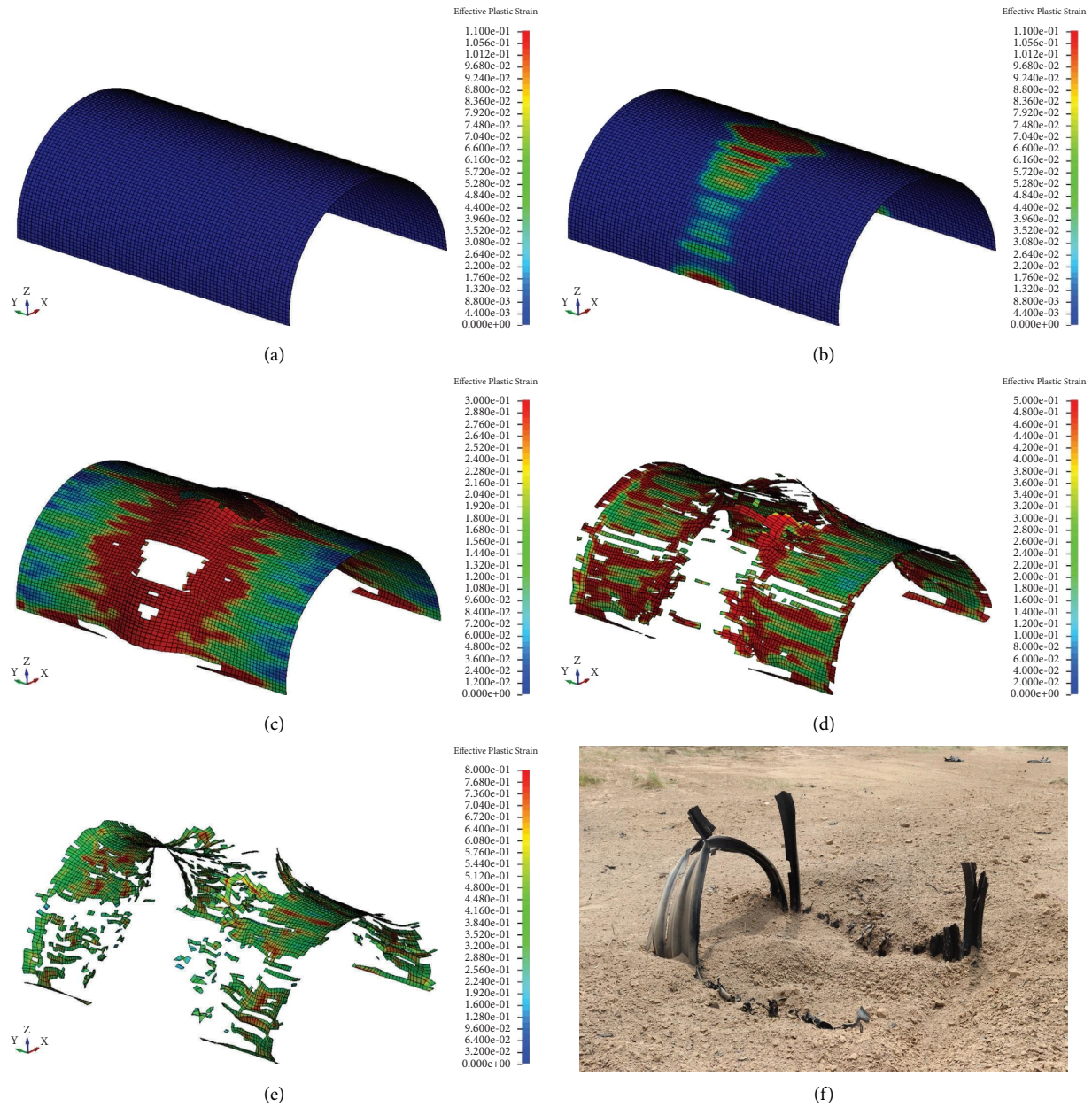


FIGURE 13: The destruction process of the pipe. (a) $T = 0$ ms. (b) $T = 0.12$ ms. (c) $T = 0.33$ ms. (d) $T = 0.57$ ms. (e) $T = 1.14$ ms. (f) The wreckage of the model after the explosion.

pipe exhibit the most severe damage, consistent with experimental findings.

5.3. Soil Scattering. The soil is indirectly defined using the `*INITIAL_VOLUME_FRACTION_GEOMETRY` keyword, which notably streamlines modeling endeavors and alleviates limitations in mesh initialization by indicating the proportions of various materials within Euler background meshes [42]. The soil modeling process is depicted in Figure 14. Initially, the entire ALE part is filled with air, followed by replacing the material within the designated container with soil. Subsequently, the soil within the designated area is replaced with air. Notably, the `CNTTYP`

value in the keyword is sequentially set to 5, 4, and 3 throughout the modeling process, defining the geometric shape of the container as cuboid, cylinder, and plane, respectively. Furthermore, the coordinates of the container's minimum and maximum points are input to determine its volume. For further details, consult the manual [31].

Figure 15 depicts the soil scattering process following the explosion. At 0.299 ms after detonation, deformation initiates at the top, with the top soil separating and dispersing at 0.899 ms, followed by deformation at the corner behind the top. Approximately 1.56 ms later, the soil at the corner is also dispersed and ejected, leading to deformation of the entire covering soil in all directions, reaching the air domain

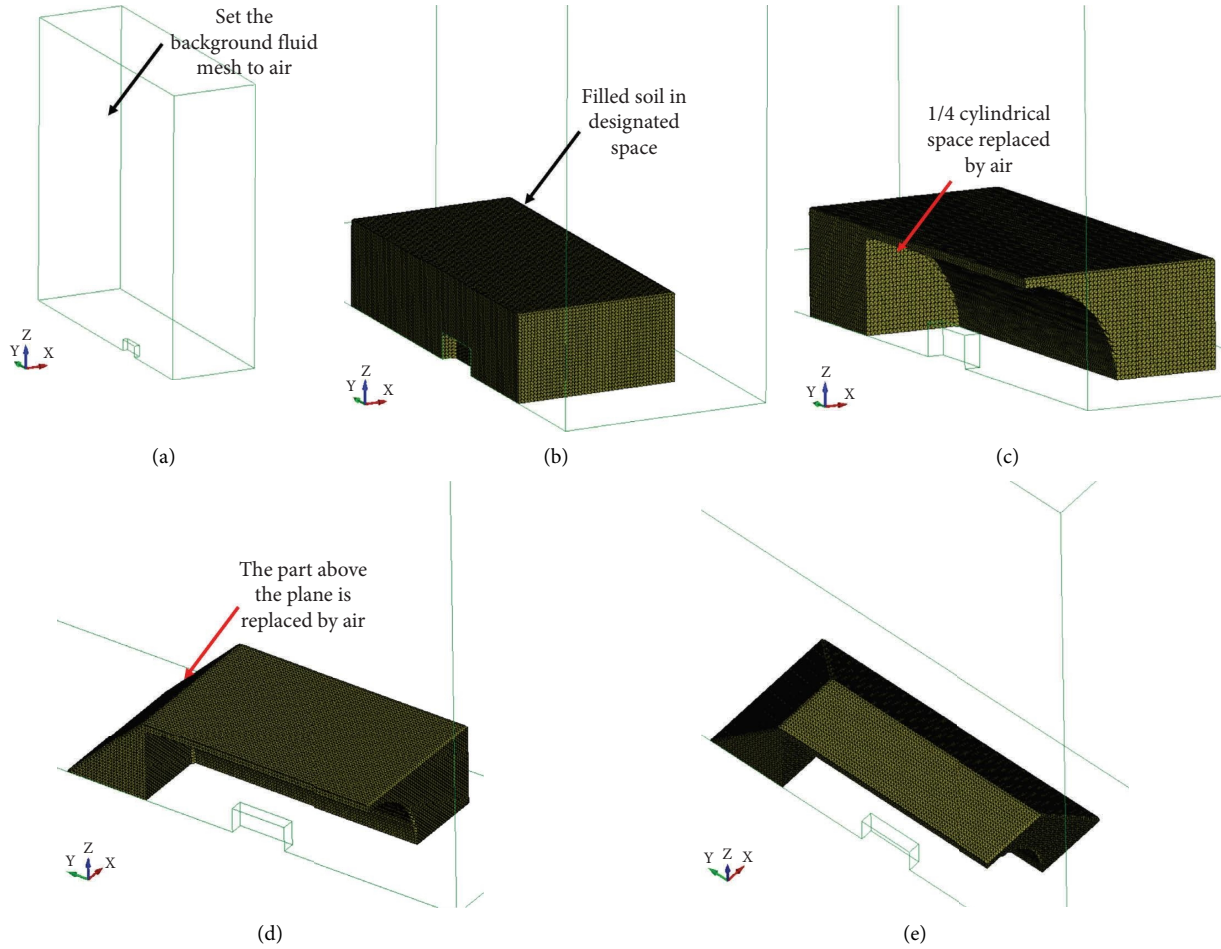


FIGURE 14: The process of soil modeling. (a) Set initial background mesh. (b) Fill soil in designated area. (c, d) Replace with air. (e) Modeling completed.

boundary at 5.76 ms. The model demonstrates more intense soil scattering in the 90° direction compared to the 180° direction, consistent with high-speed photos (Figure 9) and validating the numerical simulation.

5.4. Shockwave Propagation. Figure 16 illustrates the process of shock wave transmission. Initially, emanating from the aperture, the shock wave encounters an unobstructed trajectory. The shock waves reach the top and the rear at 0.09 ms and 0.18 ms, respectively. Subsequently, interaction with the soil causes reflected waves to become apparent from 0.6 ms to 0.81 ms, as evidenced by the increased area of the red pressure zone in the figure. At 1.50 ms, two distinct shock wave fronts emerge at the top and corner, converging into a single wave front at 3.99 ms and propagating uniformly through the air. Finally, by 5.98 milliseconds, the shockwave extends to the boundary of the air domain.

5.5. Energy Absorption of the Soil. Energy data in LS-DYNA are output in the d3hsp and glstat files, and the simulation's energy change follows the energy conservation equation [43]:

$$E_{\text{kin}} + E_{\text{int}} + E_{\text{si}} + E_{\text{rw}} + E_{\text{damp}} + E_{\text{hg}} = E_{\text{kin}}^0 + E_{\text{int}}^0 + W_{\text{ext}}, \quad (10)$$

where E_{kin} is the current kinetic energy, E_{int} is the current internal energy, E_{si} is the current sliding interface energy (including friction), E_{rw} is the current rigid wall energy, E_{damp} is the current damping energy, E_{hg} is the current hourglass energy, E_{kin}^0 is the initial kinetic energy, E_{int}^0 is the initial internal energy, and W_{ext} is the external work.

It is important to note that damping energy, sliding energy, and external work are not considered in this numerical simulation. The dissipation of energy upon the shock wave's arrival at the air boundary is incorporated into the erosion energy calculation, which is output in the bndout file. The system starts with a total kinetic energy of 0. The initial internal energy comprises the combined internal energies of both the air and the explosive. These energies are obtained from the given numerical simulation parameter E_0 , respectively. Various energy change curves are plotted as shown in Figure 17.

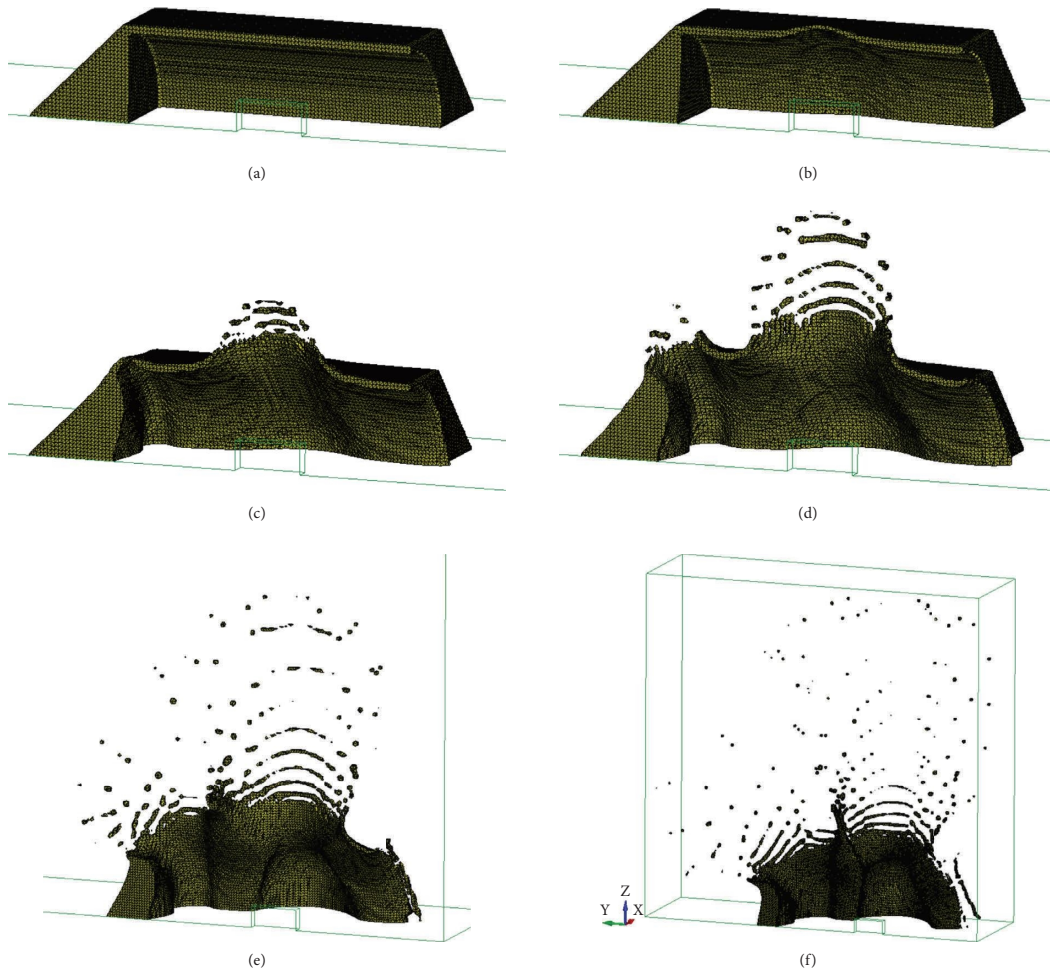


FIGURE 15: Process of soil scattering. (a) $T=0$ ms. (b) $T=0.299$ ms. (c) $T=0.899$ ms. (d) $T=1.56$ ms. (e) $T=3.18$ ms. (f) $T=5.76$ ms.

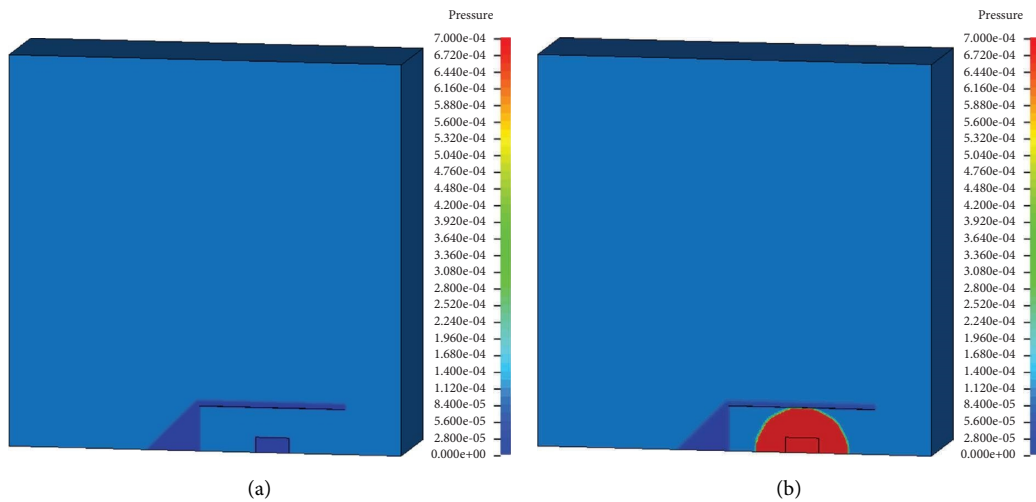


FIGURE 16: Continued.

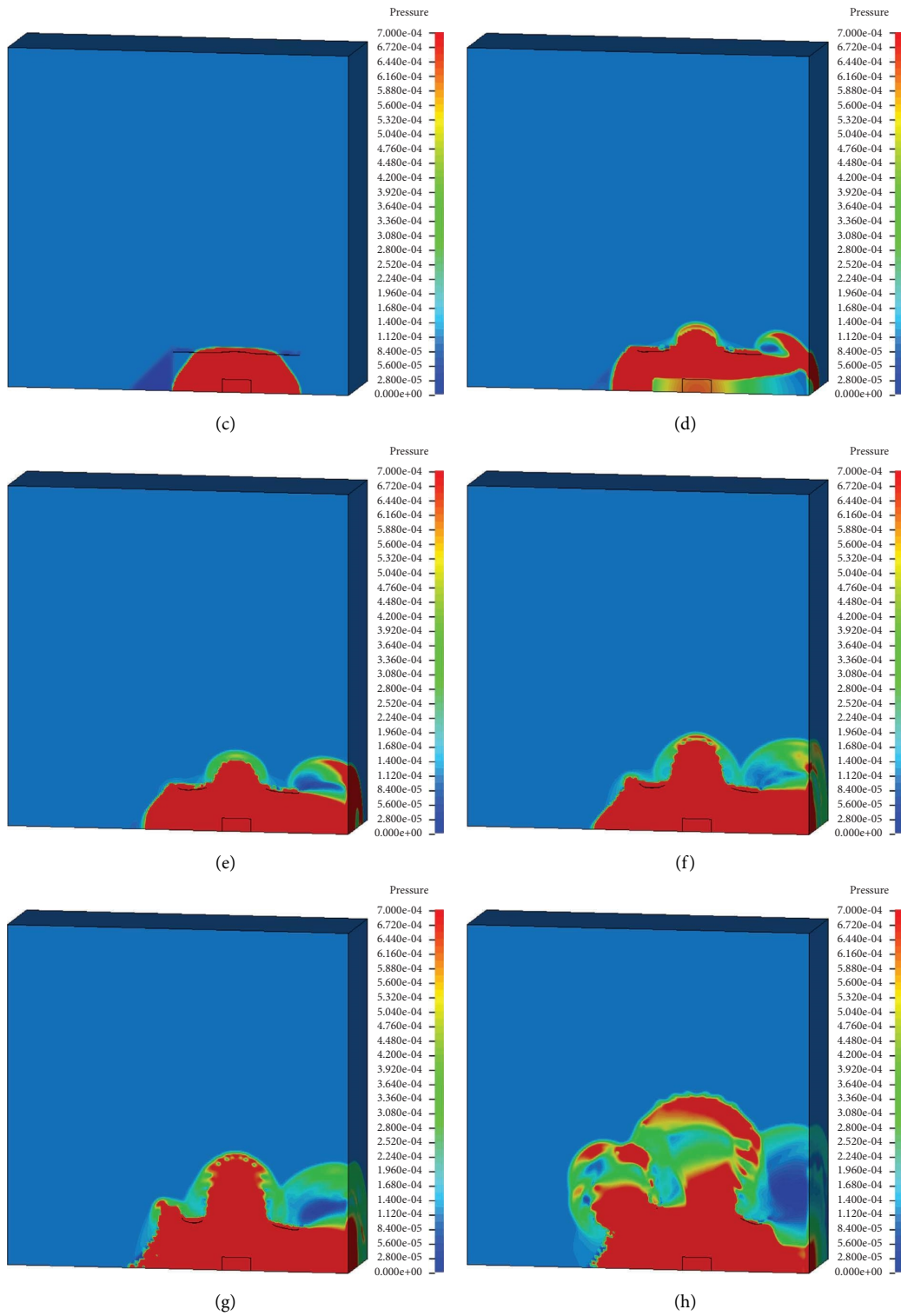


FIGURE 16: Continued.

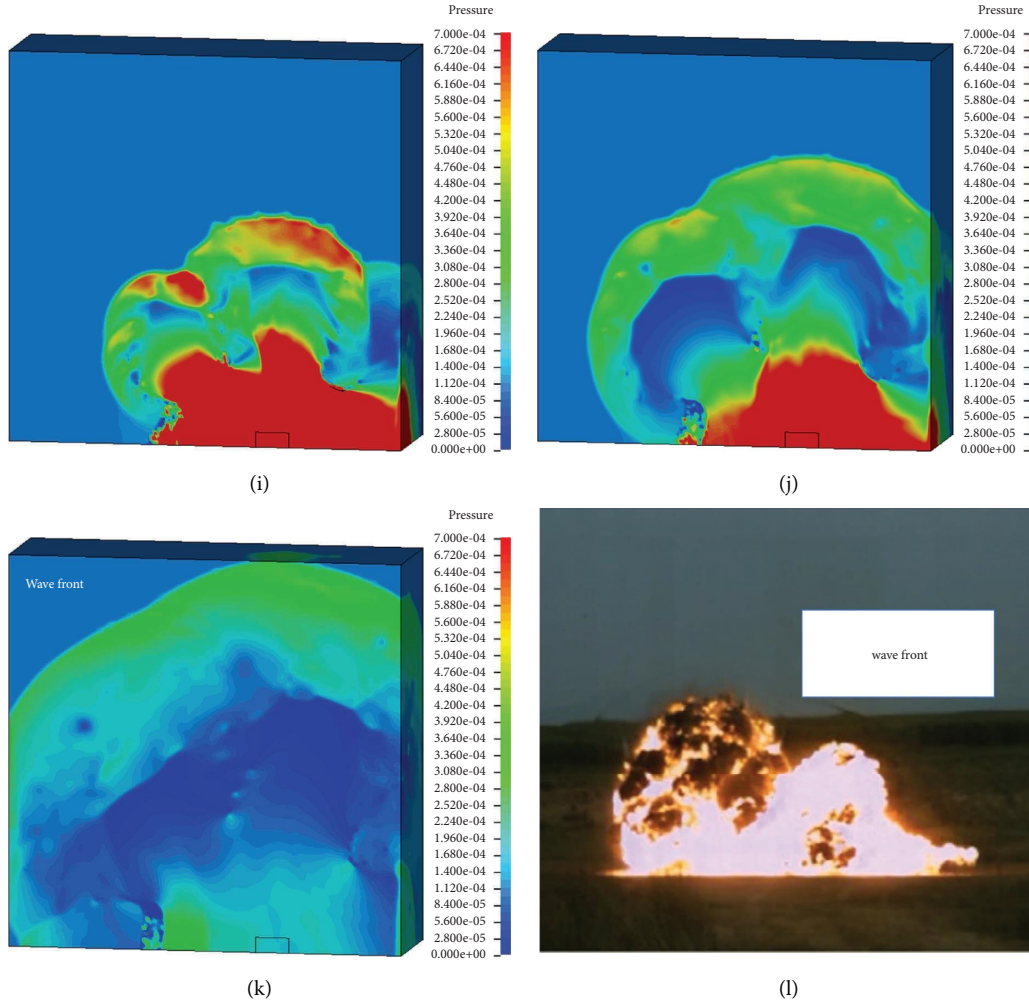


FIGURE 16: Propagation process of shock waves. (a) $T = 0$ ms. (b) $T = 0.09$ ms. (c) $T = 0.18$ ms. (d) $T = 0.6$ ms. (e) $T = 0.81$ ms. (f) $T = 1.17$ ms. (g) $T = 1.50$ ms. (h) $T = 2.49$ ms. (i) $T = 2.97$ ms. (j) $T = 3.99$ ms. (k) $T = 5.97$ ms. (l) The high-speed photo obtained from the test.

The analysis reveals that the initial internal energies of air and explosives are 1.07×10^7 J and 6.30×10^7 J, respectively. By 0.39 ms, the total energy decreases to 7.07×10^7 J. Both the pipe's kinetic and internal energies are minimal, with an hourglass energy of only 6.12×10^3 J. Importantly, the energy loss due to reduced integration in the display analysis is negligible, as it differs by four orders of magnitude from the total energy. Despite inevitable iterative errors and boundary condition influences in the numerical simulation's iterative calculation process, the energy loss remains unavoidable. The energy ratio in this numerical simulation stands at approximately 95.9%, ensuring energy conservation within an acceptable range.

Building upon this, energy-time curves for soil with varying thicknesses (ranging from 30 to 4800 mm) were generated, as depicted in Figure 18. Analysis reveals that the energy absorption value of the soil layer is approximately 8.0×10^6 J. Moreover, as the soil thickness increases, the spacing between adjacent horizontal data sections

decreases. For further analysis, a soil thickness of 30 mm is established as the reference point, with the equation defined as follows:

$$\eta = \frac{d}{30\text{mm}}, \quad (11)$$

where η is the proportional multiple of soil thickness and d is the rear soil thickness.

To depict the energy absorption rate of the soil, a functional relationship between η and the absorbed energy by the soil is established. The data points are fitted, resulting in fitted curves and relations with 96% confidence, as illustrated in Figure 19. The fitted equation for the data takes the form of a logarithmic function with a second-order derivative less than 0, indicating a decreasing energy absorption rate of the soil. This suggests the existence of a suitable design value for the thickness of the rear cover soil that can satisfy both safety distance requirements and

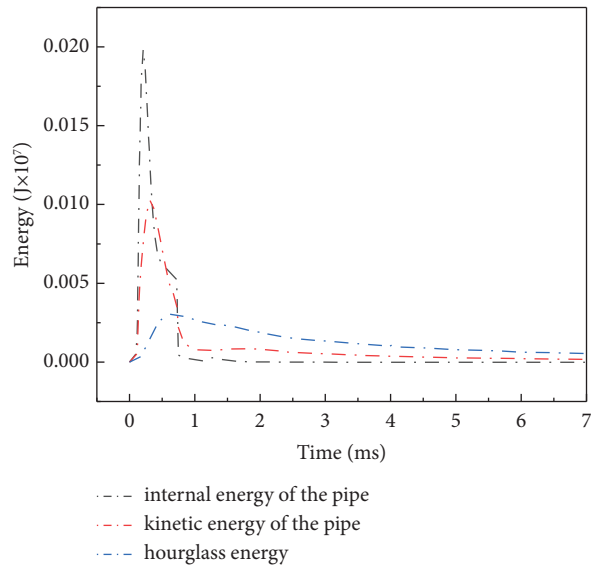
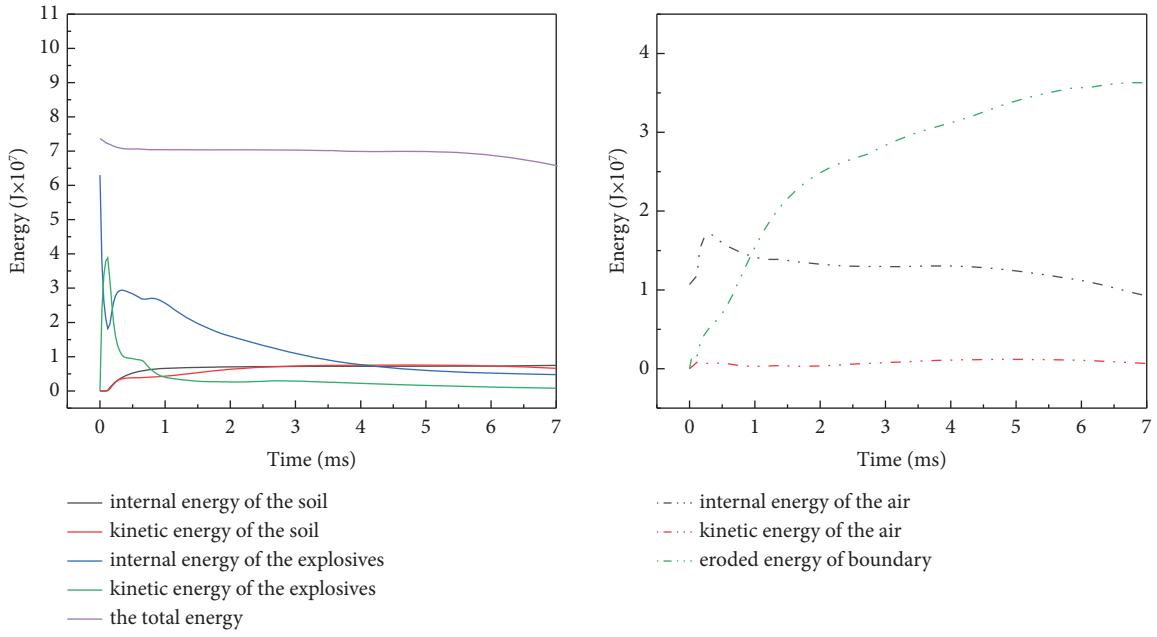


FIGURE 17: Each energy change curve.

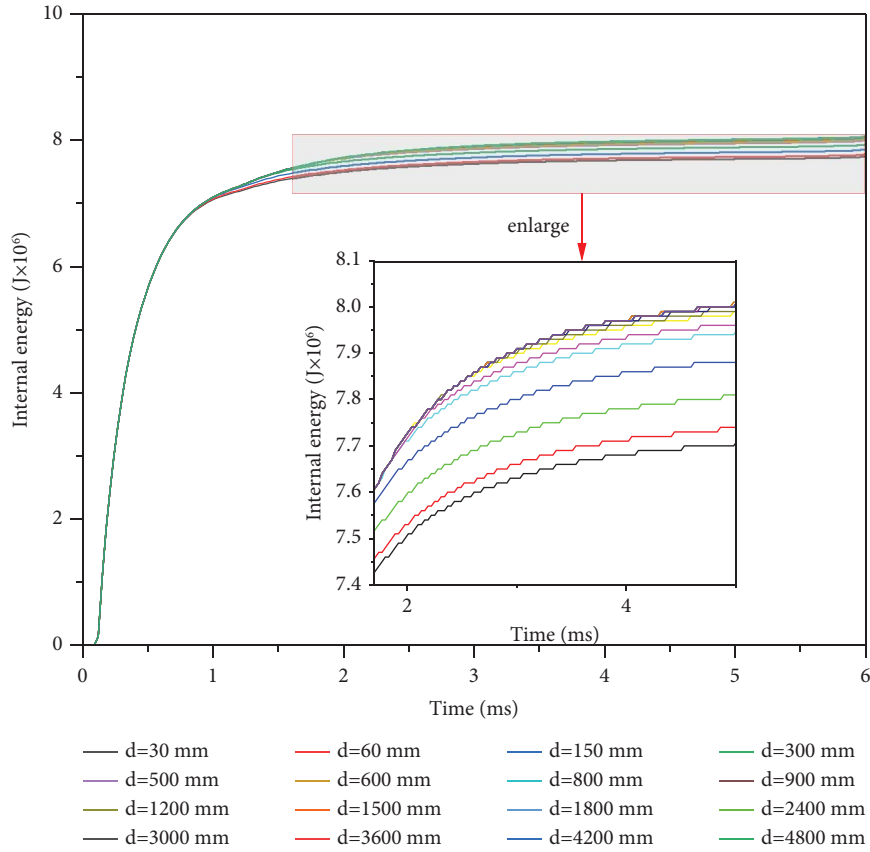


FIGURE 18: Energy absorption curve of soil.

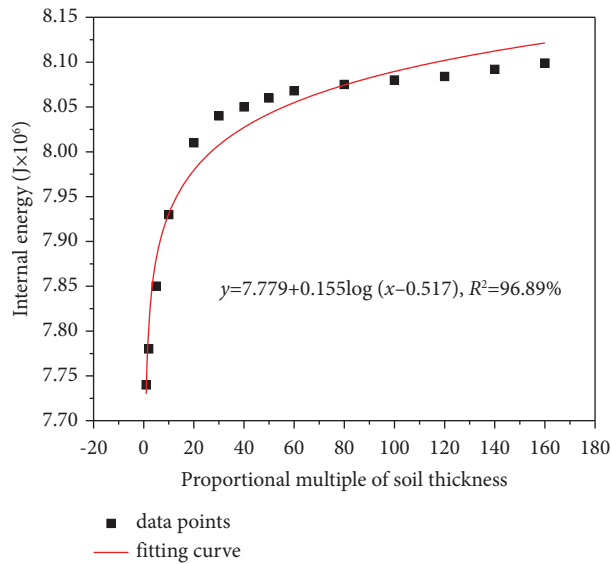


FIGURE 19: Proportional multiple-energy fitting curve.

engineering construction costs simultaneously. Further research is warranted to determine the optimal design value of the soil cover thickness.

6. Conclusion

In this paper, both explosion experiments and simulations were undertaken to explore the propagation of external pressure and assess the influence of rear soil thickness on an earth-covered magazine during internal explosions. The primary findings are summarized as follows:

- (1) With an increase in the thickness of the earth covering behind the model compared to a rear soil thickness of 30 mm, significant reductions are noted in both air pressure surges and positive phase impulses. Specifically, in the near zone of the explosion, air overpressure decreases by approximately 22%, accompanied by a 6% decrease in positive phase impulse. Similarly, in the far zone, there is a significant decrease of about 39% in air overpressure, coupled with a 24% decrease in positive phase impulse. These findings underscore the effectiveness of augmenting rear soil thickness in mitigating blast shock wave damage.
- (2) The disposal of soil from the model exhibits significant nonuniform characteristics, with soil accumulation primarily concentrated in a T-shaped area spanning $\pm 90^\circ$ and 180° . The soil absorbs approximately 8.0×10^6 J of energy, representing roughly 10.85% of the cumulative internal energy within the system. Moreover, as the rear soil thickness increases, the energy absorption rate of the soil decreases.
- (3) The outcomes of the numerical simulations closely match the measured test results, affirming the credibility of the model. This alignment serves to affirm the precision and dependability of the model. Additionally, the ALE fluid-structure coupling algorithm proves highly effective in accurately simulating the experimental procedure for conducting internal explosion tests on the model of the earth-covered magazine.

Data Availability

The data used to support the findings of this study are included within the article.

Conflicts of Interest

The authors declare that they have no conflicts of interest or personal relationships that could have appeared to influence the work reported in this paper.

Acknowledgments

This research work was financially supported by the Postgraduate Scientific Research Innovation Project of Hunan Province (Grant no. XDCX2020B135) and the Postgraduate Scientific Research Innovation Project of Hunan Province (Grant no. CX20210648).

References

- [1] GB, *Safety Standard for Design of Underground and Earth-Covered Powder and Explosive Magazine*, China Planning Press, Beijing, China, 2009.
- [2] C. R. L. Mann, "Model igloo magazine explosion tests," Naval Proving Ground, Arco, Idaho. Armed Services Explosives Safety Board, Washington, DC, USA, Technical Paper No. 4, 1947.
- [3] S. W. Thompson, "Igloo tests," Naval Proving Ground, Arco, Idaho. Armed Services Explosives Safety Board, Washington, DC, USA, Technical Paper No. 3, 1947.
- [4] C. N. Kingery, G. A. Coulter, and G. T. Watson, "Blast parameters from explosions in model earth covered magazines," BRL Memorandum Report No. 2680, Defense Technical Information Center, Fort Belvoir, VA, USA, 1976.
- [5] DoD, *Structures to Resist the Effects of Accidental Explosions (UFC 3-340-02)*, USA Army Corps of Engineering, Washington DC, USA, 2008.
- [6] GB, *Safety Standard for Design of Engineering of Civil Explosive Materials*, China Planning Press, Beijing, China, 2018.
- [7] M. Beppu, T. Ohno, M. Shiomi, and M. Katayama, "The effect of thickness of covered soil on the properties of blast wave pressure on site due to inner explosion in an earth covered RC explosives magazine," *Journal of Structural Engineering A*, pp. 1022–1033, 2008.
- [8] Z. Liu, G. Xu, C. Gong, and Y. Qiu, "Analysis of critical factors in the safe distance of earth-covered ammunition depot," *Protective Engineering*, vol. 43, no. 06, pp. 22–28, 2021.
- [9] X. Li, Z. Liu, O. Huang, and Y. Qiu, "Discussion on influencing factors of ground ammunition depot safety distance and protective measures," *Protective Engineering*, vol. 45, no. 01, pp. 39–47, 2023.
- [10] G. Xu, Y. Qiu, O. Huang, F. Zhang, X. Li, and Z. Zhang, "Study of the propagation of external pressure on soil-covered depot," *Protective Engineering*, vol. 44, no. 01, pp. 22–28, 2022.
- [11] G. Xu, Y. Qiu, H. Xing, X. Li, and C. Gong, "Experimental and numerical investigation of internal explosion in an earth-covered magazine," *Buildings*, vol. 12, no. 11, p. 1872, 2022.
- [12] M. Steyerer and O. Stange, "DEU ammunition storage in earth covered ISO-Containers," in *Bundeswehr Technical Center for Protective and Special Technologies (WTD 52) 83458 Schneizlreuth*, Germany, July 2010.
- [13] L. Tian and P. Deng, "Surface overpressure distribution and dynamic response of the retaining wall of the underground structure subjected to inner explosion," *Advanced Materials Research*, vol. 790, pp. 396–400, 2013.
- [14] I.-T. Wang, "Numerical and experimental approach for failure analysis of soil subjected to surface explosion loading," *Shock and Vibration*, vol. 2021, pp. 1–12, 2021.

- [15] W. D. Kovacs, H. B. Seed, and C. K. Chan, "Dynamic moduli and damping ratios for a soft clay," *Journal of the Soil Mechanics and Foundations Division*, vol. 97, no. 1, pp. 59–75, 1971.
- [16] Z. Wang, H. Hao, and Y. Lu, "A three-phase soil model for simulating stress wave propagation due to blast loading," *International Journal for Numerical and Analytical Methods in Geomechanics*, vol. 28, no. 1, pp. 33–56, 2003.
- [17] D. Chapman, C. Braithwaite, and W. Proud, "Shock-loading of statically compacted soil," in *AIP Conference Proceedings*, pp. 1367–1370, New York, NY, USA, October 2007.
- [18] Z. X. Zhang, S. Q. Kou, L. G. Jiang, and P.-A. Lindqvist, "Effects of loading rate on rock fracture: fracture characteristics and energy partitioning," *International Journal of Rock Mechanics and Mining Sciences*, vol. 37, no. 5, pp. 745–762, 2000.
- [19] Z. Wang, Y. Lu, H. Hao, and K. Chong, "A full coupled numerical analysis approach for buried structures subjected to subsurface blast," *Computers and Structures*, vol. 83, no. 4-5, pp. 339–356, 2005.
- [20] J. X. Liu and Z. F. Chen, "Experimental study on the influence of compactness and water content on the dynamic mechanical properties of compacted clay," *Rock and Soil Mechanics*, vol. 33, no. 6, pp. 1631–1639, 2012.
- [21] D. Ma, H. Xiang, Z. Zhou, Y. Tan, and X. Wang, "Study on energy dissipation characteristic of ice-rich frozen soil in SHPB compression tests," *Geofluids*, vol. 20229 pages, 2022.
- [22] V. D. Alekseenko and G. V. Rykov, "Experimental data on stress-wave parameters in the earth due to underground and surface explosions," *Journal of Applied Mechanics and Technical Physics*, vol. 9, no. 4, pp. 409–411, 1972.
- [23] M. Grujicic, B. Pandurangan, and B. A. Cheeseman, "The effect of degree of saturation of sand on detonation phenomena associated with shallow-buried and ground-laid mines," *Shock and Vibration*, vol. 13, no. 1, pp. 41–61, 2006.
- [24] M. Grujicic, B. Pandurangan, J. D. Summers, B. A. Cheeseman, W. N. Roy, and R. R. Skaggs, "Application of the modified compaction material model to the analysis of landmine detonation in soil with various degrees of water saturation," *Shock and Vibration*, vol. 15, no. 1, pp. 79–99, 2008.
- [25] M. Swisdak, J. Tancreto, and J. Tatom, "SciPan 3: debris hazards from a concrete and masonry PES and response of unreinforced masonry to blast loading," Defense Technical Information Center, Fort Belvoir, VA, USA, NAVFAC TM-2388-SHR, 2006.
- [26] C. Xiong, *Numerical Simulation of Debris Throw after Breaking up of a concrete Structure by Blast Load*, Nanyang Technological University, Singapore, 2008.
- [27] P. D. Smith, G. C. Mays, T. A. Rose, K. G. Teo, and B. J. Roberts, "Small scale models of complex geometry for blast overpressure assessment," *International Journal of Impact Engineering*, vol. 12, no. 3, pp. 345–360, 1992.
- [28] Y. Yang, X. Li, X. Wang, L. Zhang, and M. Zhang, "Scale similarity model of internal explosion in closed field," *Journal of Vibration and Shock*, vol. 33, no. 02, pp. 128–133+140, 2014.
- [29] E. Buckingham, "On physically similar systems; illustrations of the use of dimensional equations," *Physical Review A*, vol. 4, no. 4, pp. 345–376, 1914.
- [30] W. E. Baker, P. A. Cox, P. S. Westine, J. Kulesz, and R. A. Strehlow, *Explosion Hazards and Evaluation*, Elsevier, Amsterdam, Netherlands, 1983.
- [31] LS-DYNA, *LS-DYNA Keyword User's Manual*, Livermore Software Technology Corporation, California, CA, USA, 2007.
- [32] J. Wang and M. S. Gadala, "Formulation and survey of ALE method in nonlinear solid mechanics," *Finite Elements in Analysis and Design*, vol. 24, no. 4, pp. 253–269, 1997.
- [33] H. C. Stoker, *Developments of the Arbitrary Lagrangian-Eulerian Method in Nonlinear Solid Mechanics*, University of Twente, Enschede, Netherlands, 1999.
- [34] A. Haufe, K. Weimar, and U. Göhner, "Advanced airbag simulation using fluid-StructureInteraction and the eulerian method in LS-DYNA," in *Proceedings of the LS-DYNA Anwenderforum*, Deutschland, December 2004.
- [35] Y. S. Tai, T. L. Chu, H. T. Hu, and J. Y. Wu, "Dynamic response of a reinforced concrete slab subjected to air blast load," *Theoretical and Applied Fracture Mechanics*, vol. 56, no. 3, pp. 140–147, 2011.
- [36] T. Wu, N. Jiang, C. Zhou, X. Luo, H. Li, and Y. Zhang, "Experimental and numerical investigations on damage assessment of high-density polyethylene pipe subjected to blast loads," *Engineering Failure Analysis*, vol. 131, Article ID 105856, 2022.
- [37] J. Wang, "Simulation of landmine explosion using LS-dyna3d software: benchmark work of simulation of explosion in soil and air," *Defence Science and Technology Organisation*, 2001.
- [38] G. Liu, Y. Zhang, and M. Xiao, "Numerical simulation analysis of combined seismic response for rock-lining-water in hydraulic tunnel," *Shock and Vibration*, vol. 2021, Article ID 5547222, 11 pages, 2021.
- [39] M. Zhang, "Numerical analysis for dynamic response of in situ blasting expansion of large cross-section tunnel with small net distance," *Advances in Civil Engineering*, vol. 2021, Article ID 2896782, 7 pages, 2021.
- [40] Y. X. Zhai, H. Wu, and Q. Fang, "Impact resistance of armor steel/ceramic/UHPC layered composite targets against 30CrMnSiNi2A steel projectiles," *International Journal of Impact Engineering*, vol. 154, Article ID 103888, 2021.
- [41] H. Wang, Y. Zhao, R. Shan, X. Tong, and D. Liu, "Analysis of blasting vibration effect of railway tunnel and determination of reasonable burial depth," *Geofluids*, vol. 2022, Article ID 7151294, 8 pages, 2022.
- [42] S. Shi, Y. Liao, X. Peng, C. Liang, and J. Sun, "Behavior of polyurea-woven glass fiber mesh composite reinforced RC slabs under contact explosion," *International Journal of Impact Engineering*, vol. 132, Article ID 103335, 2019.
- [43] Ls-Dyna Support, "ls-dyna users guide: energy data [DB/OL]," 2024, <https://www.dynasupport.com/tutorial/ls-dyna-users-guide/energy-data>.